Materials Today • Volume xxx, Number xx • xxxx 2022

ELSEVIER

Intrinsic ion transport of highly charged sub-3-nm boron nitride nanotubes

Aaditya Pendse [1], Semih Cetindag [2], Kun Wang [1], Donglin Li [1], Richard J. Castellano [2], Da-Chi Yang [2], Tongshuai Wang [1], Jerry W. Shan [2,*], Sangil Kim [1,*]

[1] Department of Chemical Engineering, University of Illinois at Chicago, Chicago, IL 60607, USA
[2] Department of Mechanical and Aerospace Engineering, Rutgers University, Piscataway, NJ 08854, USA

Debate regarding the transport mechanisms of water and ions in highly charged one-dimensional (1D) nanochannel continues because of a lack of available experimental data. Here, we present a nanofluidic platform consisting of ≈2.7-nm-diameter boron nitride nanotubes (BNNTs) as a model system, and report the experimental ion transport in these sub-3-nm BNNTs. We elucidate that strong electrostatic interactions between the highly charged tube walls and ions, stemming from the high surface-charge density (378 mC/m^2) of BNNTs, play important roles in defining the ion transport mechanism in BNNT pores. Experimental analysis of ion transports supported by numerical the Donnan steric pore model with dielectric exclusion (DSPM-DE) and Derjaguin–Landau–Verwey–Over beek (DLVO) model elucidate the relationship of the ionic charge density and surface-charge density of the BNNT wall to electrostatic interaction, steric, and dielectric effects. We also demonstrate that BNNTs exhibit higher NaCl separation (≈90%) than commercial reverse-osmosis (≈80%) and nanofiltration (≈60%) membranes under the same experimental conditions, despite having a larger pore size. Our results establish design criteria for developing highly efficient ion-selective membranes for various practical applications.

Keywords: Boron nitride nanotubes; Ion transport; Ion selectivity; Nanofluidic; 1D nanotubes

Introduction

Designing, evaluating, and developing next-generation membrane materials for desalination or energy conversion/storage systems requires a detailed understanding of ion transport in nanopores, particularly with respect to the combination of strong confinement and surface properties on the nanoscale [1]. Many research groups have investigated novel ion transport mechanisms in various 1D nanofluidic channels (e.g., SiO_2 [2], carbon nanotubes (CNTs) [3–5], and graphene [6,7]), and particular interest has been paid to gaining a molecular-scale understanding of how the physicochemical properties of nanopores affect water and ion transport, and relate to membrane separation performance. Among several 1D nanofluidic channel materials, CNTs have been widely used to fabricate nanopore devices to investigate molecular transport (e.g., ions, water, or DNA) in nanoconfined channels, owing to their precisely controllable pore diameters, and their well-defined 1D nanostructures and curvature, which are hardly observed in 2D nanochannels [3–5,8–10]. Many experimental and theoretical studies have demonstrated interesting curvature- and diameter-dependent phenomena of CNTs, such as fast water flow [11,12], ion selectivity, and rapid proton conduction [13], all of which can arise from the unique water structures in curved 1D nanochannels. However, understanding of the ion-transport properties is more desirable for a highly charged nanotubes than for inert hydrophobic

* Corresponding authors.
E-mail addresses: Shan, J.W. (jshan@soe.rutgers.edu), Kim, S. (sikim@uic.edu).

 https://doi.org/10.1016/j.mattod.2022.09.006

Please cite this article in press as: A. Pendse et al., Materials Today (2022), https://doi.org/10.1016/j.mattod.2022.09.006

channels, such as pristine graphene and CNTs, because the water flux and ion transport are controlled by complex interactions at the water-channel and ion-channel interfaces, as well as between water and ions, which together strongly affect the water occupancy and ion distribution in nanopores. Recently, several molecular simulation studies have suggested that BNNTs, which share the crystallographic structure of CNTs but have radically different electronic properties [14], show great potential for highly efficient water and ion transport [15]. Among the few experimental studies on mass transport through BNNTs, Secchi et al. have recently observed no slippage of the pressure-driven water flow rate in 14-nm-diameter BNNTs, in contrast to the radius-dependent surface slippage observed in CNTs [16]. However, the highly charged BNNT surface is expected to show unique ion and water transport properties near the sub-continuum region, owing to the prominent contributions of surface-charge-driven nanoflows. Furthermore, the effects of surface wettability on the transport behavior of confined ions and molecules becomes increasingly prominent under 10-nm pore diameters [17]. Although several studies reported ion transport properties in 2D BN nanochannels [18,19], both the effect of nanoconfinement and curvature, and charged groups in nanochannels should be considered together to understand the interaction of ionic species in nanopores and rationally design the nanostructred membranes that can provide high separation performance.

Here, we report the experimental ion transport in ≈2.7-nm-diameter BNNT arrays as a nanofluidic platform (Fig. 1a). We compared the ion-transport properties of the charged BNNTs with those of ≈2.7-nm-diameter CNTs, which lack strong elec-

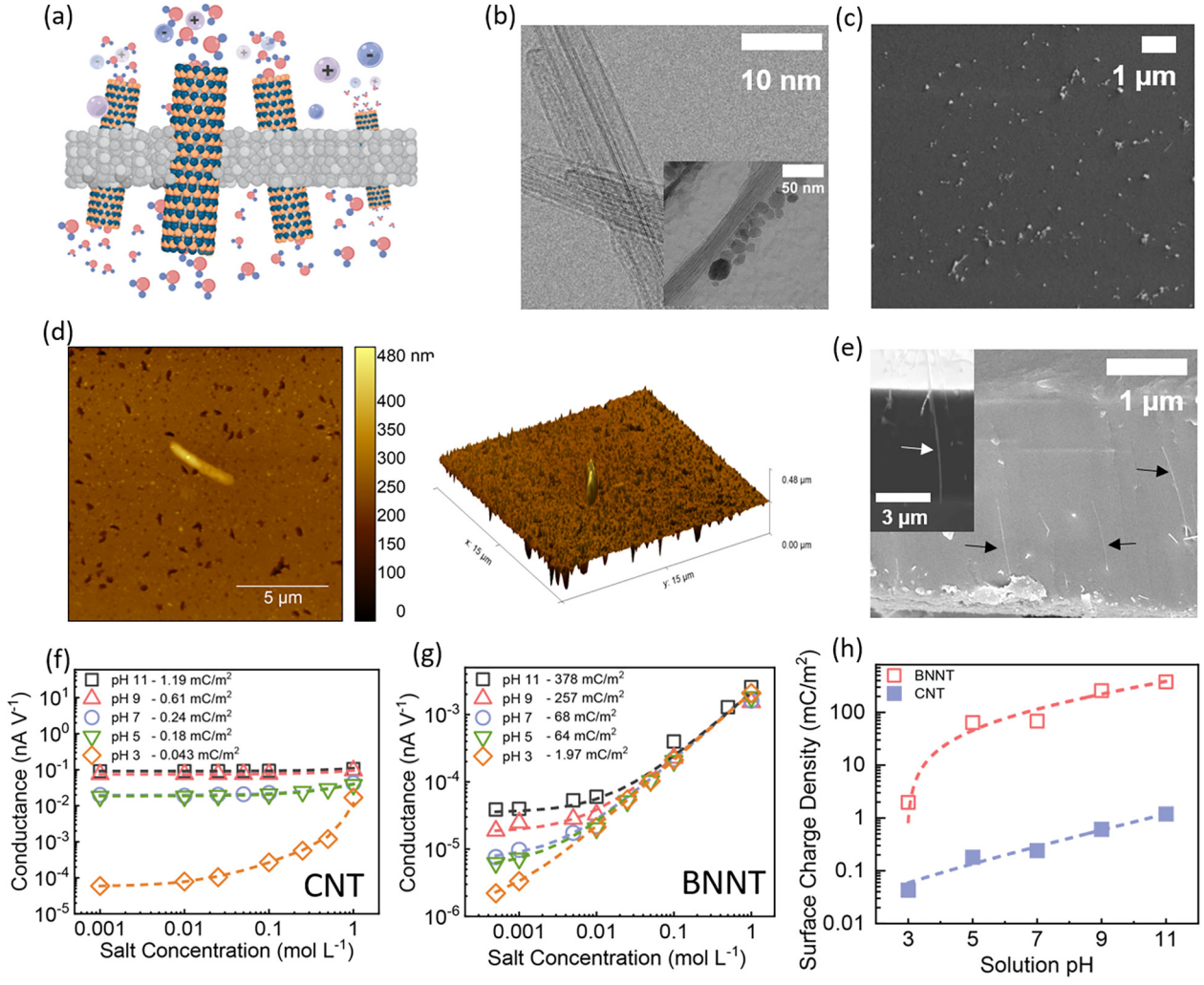

FIGURE 1

(a) Schematic illustration of the ion-transport mechanism through the BNNT nanofluidic platform. (b) High-resolution transmission-electron-microscopy images of BNNTs. Inset shows the Fe_3O_4 nanoparticles attached to the nanotube walls. (c) Top-view SEM image showing the nanotube distribution over the BNNT platform. (d) (left) AFM image of the vertically aligned BNNTs protruding from the polymer–matrix surface. (right) 3D topography AFM image on the left. (e) Cross-sectional SEM image showing aligned BNNTs across the platform cross-section and spanning the cross-section as ion-conductive channel (inset). Arrow indicates the aligned nanotube in polymer matrix. Portions of the aligned BNNTs are visible on the cleaved cross-sectional surface, while other portions remain embedded in the matrix. Conductance versus salt concentration for the (f) BNNT and (g) CNT platforms at different pH values: pH 3 (gray open squares), pH 5 (yellow open squares), pH 7 (green open squares), pH 9 (red open squares), and pH 11 (blue open squares). Dotted lines represent the theoretical fit according to the conductance equation. (h) Surface–charge density of the BNNT (red open squares) and CNT devices (blue open squares) for pH 3–11.

Please cite this article in press as: A. Pendse et al., Materials Today (2022), https://doi.org/10.1016/j.mattod.2022.09.006

trostatic interactions between ions and inert graphitic carbon walls. The BNNT nanopores showed higher rejection performance for various ion species and dyes than the CNT pores. We also employed numerical models to show that the superior ion-separation properties of BNNT pores originate mainly from Donnan exclusion effects, with minor contributions of steric and dielectric effects. In addition, we demonstrate that BNNT arrays can outperform commercial reverse osmosis (RO) and nanofiltration (NF) membranes, owing to their high electrostatic interactions against ions.

Experimental methods

Materials

Few-walled BNNTs were purchased from BNNT LLC, USA, and the iron-oxide nanoparticles suspended in ferrofluid were obtained from EMG 605 Ferrotec USA Corporation. Carbon nanotubes were purchased from Chasm Technologies Inc. UV-curable acrylated polyurethane oligomer (SU-710) was purchased form Soltech, Ltd, and Darocur 1173 photoinitiator was purchased from BASF Corp. Pyrenetetrasulfonic acid tetrasodium salt (Na_4PTS), potassium ferricyanide ($K_4Fe(CN)_6$), 2,6-naphthalene-di-sulfonic acid disodium salt (NDS), sodium chloride (NaCl), ruthenium-tris(2,2′-bipyridyl) dichloride (99.9%), sodium chloride (NaCl), sodium nitrate ($NaNO_3$), potassium chloride (KCl), potassium hydroxide (KOH), and hydrochloric acid (37% wt/wt) were purchased from Sigma Aldrich. Sodium fluoride (NaF) and sodium bromide (NaBr) were purchased from Ward's Science. Direct Blue 71 (≥50%), Congo Red (≥78.8%), and Acid Orange 7 (≥90%), were purchased from Sigma Aldrich. Acid blue 92 dye (≥99%) was purchased from Tokyo Chemical Industry Co., Ltd. (TCI–America). All chemicals were used without further purification, and the aqueous solutions were prepared with Barnstead NANOpure deionized water (DI) (18.2 MΩ cm). The reverse osmosis (RO) membrane (UTC-82 V) and nanofiltration (NF) membrane (Filmtec-NF270) were obtained from Toray Inc. and Dow Inc., respectively, and Table S1 provides their technical specifications.

Characterization of BNNT and CNT

Fig. S1 shows Raman spectroscopy data of the CNT and BNNT used in the array fabrications. As shown in Fig. S1a, the CNTs are well-graphitized with a G (1590 cm^{-1}) to D (1310 cm^{-1}) band ratio as high as ≈18 and a noticeable radial breathing mode. Fig. S1b indicates that Raman spectrum of the BNNT shows a strong peak at 1366 cm^{-1}, which corresponds to the active E_{2g} tangential mode of BNNTs. For the TEM sample preparation, we dropped suspension of nanotubes in isopropyl alcohol on copper TEM grid with carbon film and dried the nanotube bundles. The TEM images shown in Fig. 1b and Fig. S2 clearly confirmed that the CNTs and BNNTs with low defect density. Diameter distribution of CNT and BNNT were also measured from several TEM images. CNT and BNNT show diameter distributions centered at 2.72 ± 0.93 nm and 2.67 ± 1.02 nm, respectively (Fig. S3). These Raman and TEM results indicate that the CNT and BNNT used in the fabrication of nanotube arrays were high-quality nanotubes.

Fabrication of the vertically aligned BNNT and CNT nanofluidic platform

Fig. S4 illustrates the fabrication process for our nanotube nanofluidic platform. Vertically aligned BNNT and CNT arrays were fabricated with a facile solution-based method with magnetic field- and electric field-assisted alignment of nanotubes, respectively. CNT and BNNT suspensions with a concentration of 1 mg/mL were prepared in isopropanol through bath sonication for 15 min at 20 °C. The isopropanol was then evaporated and replaced by DI water, and this was followed by a 10-min bath sonication and 30-s tip sonication to obtain stable CNT and BNNT suspensions. For the CNT platform, the aligned CNT array in the urethane matrix was prepared without any further modification of CNT, by using an induced electrical dipole; alignment with the electric field was as described in our previous work [20,21]. For the BNNT platform, BNNTs were first functionalized with iron-oxide nanoparticles to enable their alignment with a magnetic field. A 40 μL volume of 10-nm iron-oxide nanoparticles in ferrofluid was added to 10 mL of BNNT dispersion. These iron-oxide particles in aqueous ferrofluid (3.9 vol%) were coated with a cationic surfactant, thus resulting in positively charged magnetic nanoparticles that could attach to the negatively charged BNNTs. This irreversible adsorption process for BNNT modification continued overnight and was followed by evaporation of DI to prepare functionalized BNNTs in powder form. Then the BNNTs were dispersed in a mixture of UV-curable acrylated polyurethane oligomer and photoinitiator (95 vol%:5 vol %). The nanotube concentration was 1.0 mg/ml. After the solution was sonicated in a bath sonicator at 50 °C for 30 min, the dispersion was placed between two Quartz ITO slides with high UV light transmission separated by two 200 μm thick spacers. A magnetic field of 1000 G was applied for 10 min to align the BNNTs while an electric field was applied to align the CNTs [20]. Then a 285 nm UV lamp (OPCO Laboratory, Inc) was used to cure the polyurethane oligomer *in situ*. The thickness of the cured nanotube/polymer composite was varied by changing the duration of UV exposure. Because the polyurethane oligomer has a relatively high UV absorption coefficient at a wavelength of 285 nm, the top 5–6 μm of liquid polymer mixture was cured with 10 s of UV exposure, thus locking vertically aligned nanotubes in position and creating a solid cross-linked nanotube/polymer composite array. Then a SF_6–O_2 gas mixture (1:1% mass flow rate) was used for reactive ion etching (March Instruments Inc, PX250) to remove any excess polymer layer and uncap the nanotubes. A multiple cycle approach with an etching time of 1 minute per cycle and power of 100 W was used to reduce the defects in cured polymer matrix during etching. The ion conductance of membranes was measured after every reactive ion etching cycle to monitor whether the nanotubes were opened or any possible defects/cracks of polymer matrix was developed.

Morphology characterization

The thickness of the fabricated nanotube array was measured with spectral reflectance (Filmetric F20-EXR) with a wavelength range of 400–1700 nm. A transmission electron microscope (FEI-TITAN) operated at 300 kV was used to measure the diameter, quality, and adherence of the iron oxide nanoparticles of nanotubes. The morphology of the nanotube/polymer array

Please cite this article in press as: A. Pendse et al., Materials Today (2022), https://doi.org/10.1016/j.mattod.2022.09.006

was characterized by field emission scanning electron microscopy (Hitachi S4800) at 5 kV and atomic force microscopy (AFM; TT-2, AFM Workshop) in tapping mode to investigate any structural defects, the average composite thickness, the nanotube alignments, and the nanotube dispersion density.

Pore density estimation

The total permeable pore density of the nanotube nanofluidic platform was estimated with KCl conductance tests, as described in literature [22]. To minimize the surface charge effect of the nanotubes, high concentration KCl solution at 0.5 M (Debye length of 0.43 nm) and neutral pH 7 were used, and the open pore density was calculated with the following equation:

$$G = \frac{A_{open,p}}{L_p}\left\{\left[10^3 F(\mu_{K^+} + \mu_{Cl^-})C\right] + \left[\frac{2\mu_{K^+}|\sigma|}{R_p}\right]\right\}$$

where G is the KCl conductance, $A_{open,\,p}$ is the open pore area, L_p is the pore length, F is Faraday's constant, μ_K^+ and μ_{Cl}^- are the mobilities of K^+ and Cl^- ions, respectively, C is the feed concentration, σ_w is the surface charge density of nanotubes, and R_p is the pore radius. At the high molarity of 0.5 M KCl, the ion conductance was dominated largely by bulk conductance, as a linear function of total open area.

Surface charge density measurement

The surface charge density of BNNTs and CNTs was measured through semiquantitative analysis of concentration and conductivity. We measured the ion current (I) generated through the nanotubes under an applied electric potential (ΔV) and calculated the corresponding conductance from the linear fit of the current versus voltage between −0.3 V and 0.3 V. These electric conductance values were measured as a function of the salt concentration. The theoretical conductance (G) was calculated with [23]:

$$G = 2e^2\mu C_s\frac{\pi R^2}{L} + e\mu\frac{2\pi R}{L}|\Sigma|(1+\alpha)$$

where C_s is the KCl concentration, e is the electronic charge, μ is the KCl mobility, Σ is the surface charge density on the BNNT or CNT membrane (in C/m^2), and the correction α accounts for the electro-osmotic contribution to conductance. To find the best fit of the theoretical equation in the experimental value, we varied the surface charge density value of the equation. Each measurement was repeated three times, and the average of the I–V curve was used to calculate the conductance corresponding to each KCl concentration.

Pressure-induced ion rejection measurements

The filtration experiments were performed with a dead-end stirred cell system under 1–3.5 bar, depending on the ion concentration, device type, and commercial NF/RO membrane. The effective test area was 0.196 cm^2 for the BNNT platform, 0.176 cm^2 for the CNT platform, and 15.21 cm^2 for the RO and NF membranes. The size exclusion and ion valence effects were studied with a 10 mM concentration of NaCl, NDS, $K_3Fe(CN)_6$, and Na_4PTS at pH values ranging from 5 to 11. To minimize any concentration polarization effect on the ion rejection performance of the membranes, the feed solution was constantly stirred at 200–300 rpm. The effects of the solution pH and ion concentration were analyzed with NaCl solutions at pH 5–11 and concentrations ranging from 1 mM to 500 mM. The rejection of 10 mM dye solutions (AO7, Congo red, AB92 and DB71) was measured to evaluate the influence of anion valence on the transport through the BNNTs and CNTs. The separation performance of the nanotubes toward the monovalent salts (NaCl, NaF, NaBr, and $NaNO_3$) with varying hydration energy and ionic change density, was evaluated at 10 mM and pH 3–11 and was compared with that of the commercial RO and NF membranes. The concentration of the feed and permeate solutions was analyzed with a conductivity meter (Orion Star A210, Thermo Scientific) and ion exchange chromatography (Dionex DX-500 with an AS14A IonPac column). The water permeance (L·m^{-2}·h^{-1}·bar^{-1}) was determined with the following equation:

$$J = \frac{V}{A \times t \times p}$$

where V is the volume of permeate solutions, A is the effective area of the membranes used in the nanofiltration cells, t is the testing time, and p is the applied pressure. The rejection (R) was calculated with the equation:

$$R = \left(1 - \left(\frac{C_P}{C_F}\right)\right) \times 100\%$$

where C_P and C_F are the concentrations in the permeate and the feed, respectively.

Osmotically induced rejection measurements

Osmotically induced ion rejection properties of CNTs and BNNTs were measured with a custom-built side-by-side diffusion cell. The nanofluidic platforms with effective areas of 0.196 cm^2 for BNNTs and 0.176 cm^2 for CNTs were sandwiched between the cells. The feed and permeate solutions were continuously stirred to decrease the concentration polarization near the surface of the platform. Concentrations of 10 mM NaCl, NDS, $K_3Fe(CN)_6$, or Na_4PTS at pH values ranging from 5 to 11 were used. Various concentrations of NaCl solutions ranging from 1 mM to 500 mM were used to evaluate the effects of the solution pH and feed concentration on the ion transport properties of BNNTs compared with CNTs. The solution pH was adjusted with either 1 M hydrochloric acid or 1 M potassium hydroxide solutions. Next, the diffusion of the dye solutions (AO7, Congo red, AB92 and DB71) was measured to evaluate the influence of the anion valence and the ionic size on the transport through the BNNT and CNT membranes.

The effects of the ionic charge density and the hydration energies of anion species on ion transport through the BNNTs and CNTs was measured with different monovalent salts (NaCl, NaF, NaBr, and $NaNO_3$) at 10 mM and a pH ranging from 3 to 11. Each experiment was repeated at least three times. Volumes of 15 ml salt solutions were used on the feed side in each case, with 15 ml of deionized water on the permeate side. The ionic conductivity of the permeate solution was continuously monitored with an ionic conductivity meter (Orion Star A210, Thermo Scientific). The measurement was continued for 48 h, and the permeate concentration at the end of 48 hours was used to calculate the ion rejection. The concentrations of anions and cations

Please cite this article in press as: A. Pendse et al., Materials Today (2022), https://doi.org/10.1016/j.mattod.2022.09.006

in the feed and permeate sides were analyzed with ion chromatography (Dionex DX-500 with an AS14A IonPac column).

Activation energy measurement

We determined the activation energies to quantify the effects of the feed concentration, solution pH, anion hydration energies, and anion valence on the transport through the BNNTs and CNTs, by measuring the ion permeability at different temperature intervals between 10 °C and 40 °C. The temperature of the test solution in the reservoirs of the side-by-side diffusion cell (PermeGear, Inc.) was controlled by a recirculating heater/chiller (Polystat, Cole Parmer). Activation energies were determined from the slopes of the plots determined by the following equation:

$$\ln\left(\frac{J_{solute}}{C_{feed}}\right) = \ln(B) - \frac{E_a}{RT}$$

where J_{solute} is the ion flux, C_{feed} is the feed concentration (mM), B is the pre-exponential factor, E_a is the activation energy, R is the gas constant, and T is the temperature. The ion flux (J_{solute}) at different concentrations and pH conditions was determined by measuring the permeate concentration at various time intervals through ion exchange chromatography. Additionally, the activation energy for the RO and NF membranes was measured and compared with that of BNNTs for a quantitative comparison of the energy barriers to ion transport.

Numerical model for ion transport

The Donnan steric partitioning pore and dielectric exclusion (DSPM-DE) model was adopted from Epsztein et al. [24] and modified to simulate ion transport in BNNTs and CNTs. The model runs based on a set of input parameters including nanotube charge, pore radius, kinematic viscosity, and ion diffusion coefficients, which can be found in literature (BNNT [23] and CNT [25]) and Tables S2 and S3. The DSPM-DE model assumes that nanotubes and bulk aqueous phases are a continuous medium, and electrolyte solutions are non-ideal and can be described by classical Debye–Hückel theory. The extended Nernst–Planck (ENP) equations were discretized inside the membrane by using the finite-difference scheme. The discretized ENP equations together with the other model equations were linearized to obtain a system of equations that were solved simultaneously. The linearized system of equations was based on an initial guess for the electrical potential and ion concentrations profiles, which were updated iteratively. The partitioning coefficients at the interfaces between the nanotube surfaces and the external solutions considered three separation mechanisms: steric hindrance, Donnan equilibrium, and dielectric exclusion. The influence of these mechanisms on ion transport was evaluated by analysis of the effects of the solution pH, feed concentration, hydration energy, and ion valence on the partitioning coefficients.

DLVO theory was used to qualitatively understand the interactions between charged ions and BNNT and CNT surfaces. The total ion-nanotube surface interaction energies were calculated as the summation of van der Waals and electrostatic double layer interactions according to the surface element integration model [26], which considers the total interaction energy between hydrated ions and the nanotube surface by integrating the interaction energy per unit surface area:

$$U(D) = \iint E(h)dA$$

where U is the interaction energy between the hydrated ion and nanotube surface, D is the closest distance between them, E is the interaction energy per unit area between the ion and nanotube surface, separated by a distance h, and dA is the estimated differential surface area of the ion.

We used the Hamaker expression for calculating the van der Waals and constant potential electrostatic double-layer interaction energy per unit area between the hydrated ion and nanotube surface, as given by the following equation:

$$E_{DLVO}(h) = E_{VDW}(h) + E_{EDL}(h) = -\frac{A_H}{12\pi h^2} + \frac{\epsilon\epsilon_0\kappa}{2}\left[(\psi_s^2 + \psi_m^2)(1 - \coth\kappa h) + \frac{2\psi_s\psi_m}{\sinh\kappa h}\right]$$

where A_H is the Hamaker constant, ϵ is the dielectric constant of the solvent, ϵ_0 is the dielectric vacuum permittivity, ψ_s is the surface potential of hydrated ions, ψ_m is the surface potential of charged nanotube devices, which was calculated with the experimental surface charge density values, and κ is the inverse Debye screening length, corresponding to the different concentrations.

The surface potential of hydrated ions was calculated according to Coulomb's law as follows:

$$\psi_s = \frac{q}{4\pi r\epsilon}$$

where ψs is surface potential of hydrated ions, q is the charge of the ions (1.602×10^{-19} C for monovalent ions, Na^+ and Cl^-), ϵ is the dielectric constant, and r is the radius of hydrated ions (0.358 and 0.332 nm for Na^+ and Cl^-, respectively [27]). Fig. S5 shows the interaction energy profiles between ions (Na^+ and Cl^-) and the nanotube surface.

Results and discussion

Our macroscopic nanofluidic platform was fabricated with field-aligned nanotube arrays serving as through-pores (details in Methods and Fig. S4). Briefly, BNNTs or CNTs of 2.7-nm diameter in powder form were dispersed in a liquid urethane prepolymer. For the CNT platform, the aligned CNT array in the urethane matrix was prepared with an induced electrical dipole and aligned with the electric field, as described in our previous work [20,21]. For the BNNT platform, the BNNT surface was decorated with 10–25 nm iron-oxide nanoparticles (Fig. 1b) to align the individual nanotubes under an external magnetic field. After the alignment of the nanotubes, the polymer matrix was cured with UV light, and this was followed by plasma etching (PE) to remove the excess polymer layer and open the end tips of the nanotubes. The as-fabricated nanotube platform showed no detectable ion conductance before the PE, thus indicating that the matrix was defect free and impermeable to ions. Then ion conductance of the nanofluidic platform was measured after every PE cycle to monitor nanotube opening. Top-view scanning electron microscopy (SEM) showed that the aligned nanotubes were well dispersed across the polymer matrix (Fig. 1c) without any visible defects on the polymer matrix, and AFM images confirmed an average exposed nanotube length of approximately

Please cite this article in press as: A. Pendse et al., Materials Today (2022), https://doi.org/10.1016/j.mattod.2022.09.006

0.15 μm (Fig. 1d and Fig. S6). Cross-sectional SEM images (Fig. 1e) showed vertically aligned BNNTs as ion-conductive channels spanning the polymer matrix. More high-resolution SEM images for aligned BNNTs in the polymer matrix are provided in Fig. S7. On the basis of ion-conductance measurements with 0.5 M KCl solution, the open pore densities were estimated to be $\approx 1.7 \times 10^5$ pores/cm^2. The surface-charge density of the BNNT channels was determined through semiquantitative analysis of concentration and conductance (details in Methods). The conductance curve showed saturation at low salt concentrations, a finding indicative of a charged confining surface [28]. The BNNT surface charge density (σ_{BNNT}) increased with the solution pH and reached a maximum of 378 mC/m^2 at pH 11 (Fig. 1f). An ab initio simulation study demonstrated that an activated boron site (one with a hydrogen atom bound to a nitrogen atom) can seed water dissociation on a BN surface ($BN_3 + H_2O \leftrightarrow BN_3\text{-}OH^- + H^+$) [23]. At higher pH, more hydroxyl ions are present in the solution, thereby increasing the adsorption of hydroxyl ions on the BN surface and consequently increasing the surface-charge density. In contrast, the surface-charge density of the CNT (σ_{CNT}) remained low regardless of pH, and the highest value was 1.2 mC/m^2 at pH 11 (Fig. 1g). As shown in Fig. 1h, the surface charge density of BNNTs was higher than that of CNTs by two orders of magnitude over the entire pH range. The dramatic increase in the surface charge density from pH 3 to pH 5 can be explained mainly by the enhanced adsorption of the hydroxyl group and a corresponding increase in the surface charge density beyond pKa value of BNNT (≈5.5) according to the charge regulation model [23].

To investigate the effects of the electrostatic interactions and the hydrated radii of ions on the ion-transport properties, we first tested the BNNT and CNT devices under the pressure by using ions with different valances and radii: pyrenetetrasulfonic acid tetrasodium salt (Na_4PTS; $z_-/z_+ = 4$), potassium ferrocyanide (PFCN; $z_-/z_+ = 3$), 2,6-naphthalenedisulfonic acid disodium (NDS; $z_-/z_+ = 2$), and sodium chloride (NaCl; $z_-/z_+ = 1$). As depicted in Fig. 2a, the rejection of 10 mM NaCl (anion hydrated radius, $r_{Cl}^- = 0.33$ nm) by BNNTs was ~35% at pH 5.0 and then increased to ~83% at pH 11. As the hydrated radius increased, ion rejection by the BNNTs increased and reached a maximum rejection of ~95% for Na_4PTS ($r_{PTS}^{4-} = 0.504$ nm) at pH 11. In contrast, the maximum rejection of CNTs was only ~13% for Na_4-PTS at pH 11, although the CNTs had the same pore diameter as the BNNTs (Fig. 2b). Similar to BNNTs at low pH conditions (pH 5 and 7), the CNTs showed a sharp increase in rejection as the hydrated radius increased beyond 0.45 nm for all pH conditions. When the surface-charge density of nanotubes was high ($\sigma_{BNNT} \geq 257$ mC/m^2 at pH 9 and 11), BNNTs showed a linear increase in rejection with the hydrated radius of the anion ($R \propto 4.39\, r_{anion}^-$) in all cases. In contrast, for nanotubes with lower surface-charge density (e.g., BNNTs < 70 mC/cm^2 at pH 7 and CNTs for all pH ranges), the ion rejection exponentially increased with hydrated radius of the anion, thereby indicating that the ion rejection of nanotubes with low surface-charge density is more sensitive to anion valence. Thus, the results suggest that the electrostatic interactions of ions with highly charged nanotube surfaces play an important role in determining the ion-rejection properties of nanotubes even in lower pH conditions.

To further investigate the effects of electrostatic screening of the nanotubes on the ion-transport properties, we tested the CNT and BNNT nanofluidic platforms with different ion concentrations and pH conditions (Fig. 2c). At relatively low pH (pH ≤ 7), the BNNTs showed 19–46% ion rejection for all NaCl solutions with a sharp increase up to 54–90% at pH 11, whereas the CNTs showed a poor ion-rejection performance for all NaCl concentration ranges, with a maximum rejection of only ~11% at pH 11. It has been reported that the BNNTs can provide high level of rejection of charged molecules because of the high negative surface-charge density on the BN surface [18,23]. As the pH increases, more hydroxyl ions are present in the solution, thus increasing the adsorption of hydroxyl ions on the h-BN surface. Thus, the stronger electrostatic repulsion present between the nanotube fixed charges and the mobile ions resulted in higher ion rejection at high pH. The enhancement in the ion-separation performance continued until the surface charge density reached a saturation point around pH 9, as reflected by the plateau in the ion-rejection curve after pH 9 (Fig. 1g). In contrast, the CNTs showed a somewhat linear increase in ion rejection with a slight transition between pH 7 and 9 (Fig. 2c), and the trend is also shown in Fig. 2b (pH 7 [dashed blue line] and pH 9 [dashed red line]). The CNT surface charge is associated with the dissociation of the carboxylic groups on the CNT rims, and the degree of dissociation increases with increasing pH [29]. However, the fewer dissociation sites at the CNT rim resulted in lower electrostatic repulsion and consequently less ion rejection than that of BNNTs with uniform high surface-charge density along the tube.

Several studies have suggested that ion transport through charged nanotubes could be highly sensitive to the degree of electrostatic screening (i.e., ionic strength) [30]. For a charged nanotube with a diameter ($d_{nanotube}$) larger than the ion size, significant exclusion of co-ions is expected when the Debye length (λ_D) exceeds the pore size ($\lambda_D > d_{nanotube}$). As the salt concentration increases, λ_D becomes smaller than $d_{nanotube}$, and this can decrease the ion exclusion. However, the increase in the NaCl concentration decreased 40% of the ion separation performance of BNNTs (from 92% to 54%), whereas the NaCl ion rejection of CNTs decreased by 70% (Fig. 2d). At high ion concentrations, more cations are available that can completely screen the negative charges on the CNT surface, thus resulting in low ion rejection at high feed concentrations. In contrast, the BNNTs showed a 54% rejection even at a 0.5 M feed concentration. The measured surface charge density of BNNTs at pH 11 was 0.378 C/m^2 (i.e., 1.16×10^5 charged groups per BNNT). However, the maximum number of cation in 4.2×10^4 nm^3 volume of nanotube (3-nm diameter and 6-μm length) at 0.5 M was approximately $1.06 \times 10^4 Na^+$ ions, which might not be sufficient to completely screen the excess negative charges on the BNNT surface; thus, the BNNT retained its high ion separation properties, as illustrated in Fig. 1e.

We further compared the experimental results with the predictions from the Donnan steric pore model with dielectric exclusion (DSPM-DE), which considers the relative contributions

Please cite this article in press as: A. Pendse et al., Materials Today (2022), https://doi.org/10.1016/j.mattod.2022.09.006

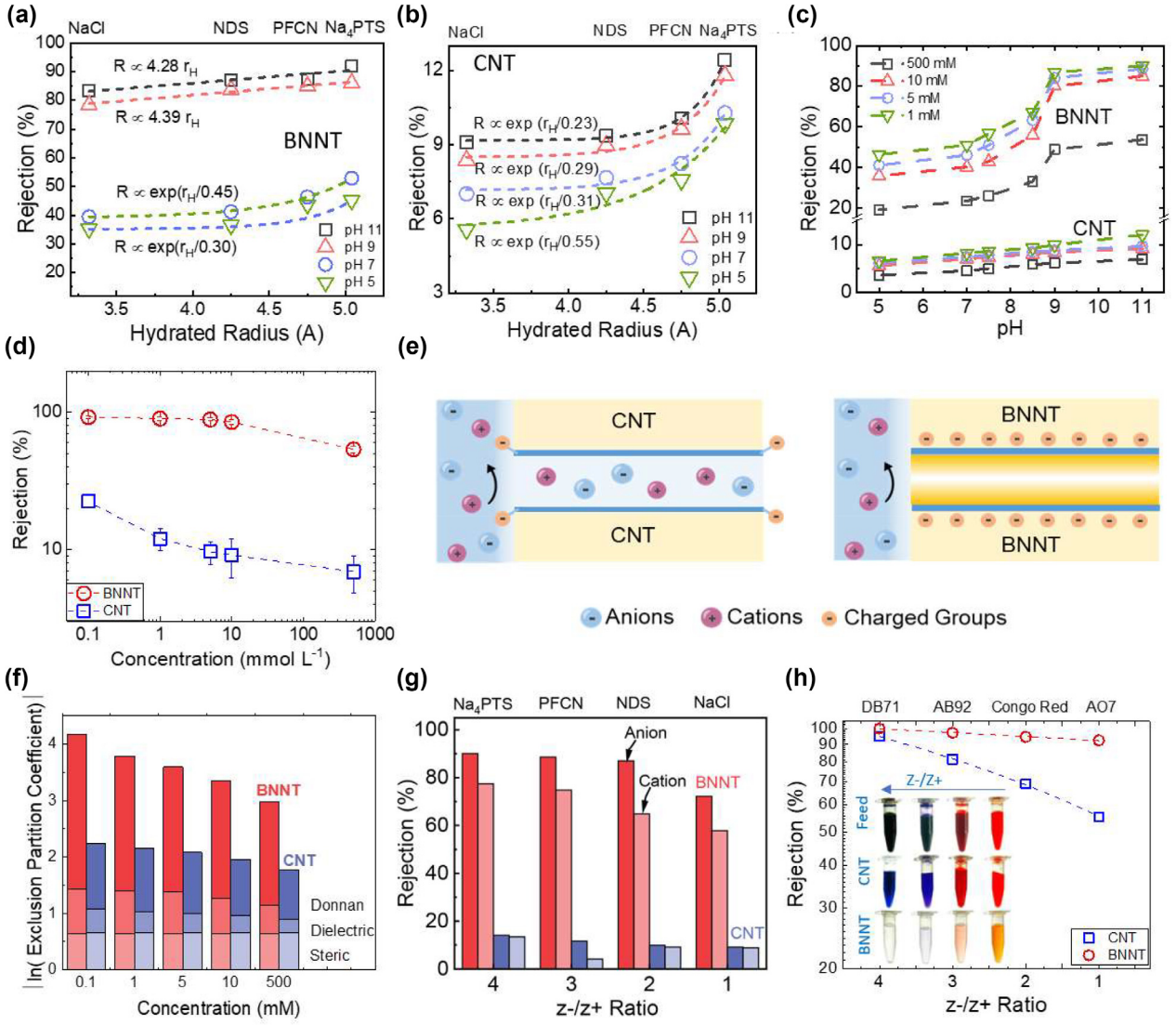

FIGURE 2

Experiments on the ion rejection properties of the (a) BNNT and (b) CNT platforms, as a function of the hydrated radius (C_{feed} = 10 mM): sodium chloride (NaCl), 2,6-naphthalene-di-sulfonic acid disodium (NDS), potassium ferricyanide (PFCN), and pyrenetetrasulfonic acid tetrasodium (Na_4PTS). Dotted lines indicate the best fits to the experimental data. (c) Pressure-induced NaCl rejection as a function of solution pH (pH 5–11) for BNNT and CNT devices. (d) Pressure-induced NaCl rejection of BNNT and CNT devices with various NaCl concentrations at pH 11. (e) Schematic illustration of the ion-rejection mechanism in BNNTs compared with CNTs. (f) DSPM–DE model analysis for BNNTs and CNTs (pH 11). The model uses extended Nernst–Planck (ENP) equations discretized inside the nanotubes, and the finite-difference scheme is used to solve for the electrical potential and ion concentration. Contributions are represented by the natural log of the absolute value of the partitioning factor for each anion, as calculated by the DSPM-DE. Experimentally measured ion rejection as a function of ion valence through BNNTs and CNTs (C_{feed} = 10 mM, pH 11) for (g) different ions and (h) dye molecules. Inset shows images of feed dye solutions, CNT permeate solutions, and BNNT permeate solutions.

of three exclusion mechanisms (steric, dielectric, and Donnan exclusions) to the ion-rejection properties of nanopores [24]. Of note, the natural logarithm value of exclusion partitioning factors indicated that larger values correlated with a greater influence on anion transport in BNNT and CNT channels. As depicted in Fig. 2f, both CNTs and BNNTs showed similar steric-exclusion partitioning factors because they had the similar pore diameter. However, the Donnan and dielectric-partitioning factors of BNNT were two times higher than those of CNTs. Additionally, the decrease in the Donnan and dielectric contributions with increasing solution ionic strength of both CNTs and BNNTs was consistent with the experimental results. By considering that the surface charges of nanotubes can greatly contribute to Donnan and dielectric effects, our model analysis confirmed that the high surface-charge density of BNNTs is the primary reason for the high ion-exclusion properties.

Fig. 2g shows the effects of anion and cation valence on the ion-rejection properties. The ion-rejection value increased with the z^-/z^+ ratio, which can be explained by the classical Donnan charge exclusion theory [31]. According to Donnan theory, ion transport in charged nanotubes is governed by the balance between the electrostatic forces of the anions and the cations. An ionic solution with a higher z^-/z^+ ratio (e.g., Na_4PTS, PFCN) experiences a stronger repulsive force from the charged surface

Please cite this article in press as: A. Pendse et al., Materials Today (2022), https://doi.org/10.1016/j.mattod.2022.09.006

groups on BNNTs, thus resulting in higher salt rejection. However, as the valence of the anion decreases, the repulsive force is not sufficiently strong to screen anions effectively, thus facilitating anion permeation and decreasing the overall salt (e.g., NaCl) rejection. In contrast, CNTs showed a minor effect of the anion valence changes on ion rejection, in agreement with the results of the pH effect (Fig. 2c). We also investigated the ion separation performance of BNNTs with large 10 mM anionic dye molecules with varying z^-/z^+ ratios: Direct Blue 71 (DB71; 3.0 nm × 1.5 nm × 1 nm), Acid Blue 92 (AB92; 1.43 nm × 1.36 nm × 0.9 nm), Congo Red (CR; 2.5 nm × 0.7 nm), and Acid Orange 7 (AO7; 0.73 nm × 1.36 nm × 0.23 nm). As shown in Fig. 2h, the BNNTs showed high dye rejection performance (R = 92%–100%), and clear or weakly colored dye solutions were collected. However, the rejection by CNTs was 95% only for DB71 and decreased to 55% for AO7 with a decrease in the z^-/z^+ ratio. These results with ion and dye solutions clearly indicated that surface–charge density has a critical role in ion and dye rejection, as predicted by the DSPM-DE model.

After the pressure-induced ion separation, we investigated the osmotically induced transport of ions in BNNTs and CNTs at different pH values (pH 5–11) more relevant to ion transport in many biological systems. Similar to the pressure-induced ion transport, the concentration-driven (C_{feed} = 0.1 mM to 500 mM and $C_{o,permeate}$ = 0.0 mM) NaCl rejection for BNNTs at different pH values showed a sharp increase from pH 7 to 9. All ion rejection by BNNT reached a maximum at pH 11, in the range of 85–90%, owing to the large increase in the surface–charge density (Fig. S8a). However, in contrast to BNNTs, CNTs showed a more linear trend in NaCl rejection with a slight transition between pH 7 and pH 9 corresponding to the surface-charge density trend of CNTs (Fig. S8b). We also tested the ion rejection of the nanotube platforms with ions of different hydrated radii to evaluate the contributions of the steric and charge effects to the osmotically induced rejection (Figs. S8c and S8d). The results were in strong agreement with those of the pressure-induced flow tests, thereby confirming a prominent role of the charge–exclusion effects on ion transport in nanotubes under both pressure-induced and osmotically induced flow conditions. The results of DSPM-DE analysis for osmotically induced flow also closely followed the pressure-induced DSPM-DE model, which indicated the strong dependence of ion transport on electrostatic interactions (Fig. S9).

To further investigate the hindrance of ion transport through the nanotubes, we measured the osmotically induced ion rejection and activation energies of Na_4PTS, PFCN, and NaCl at differ-

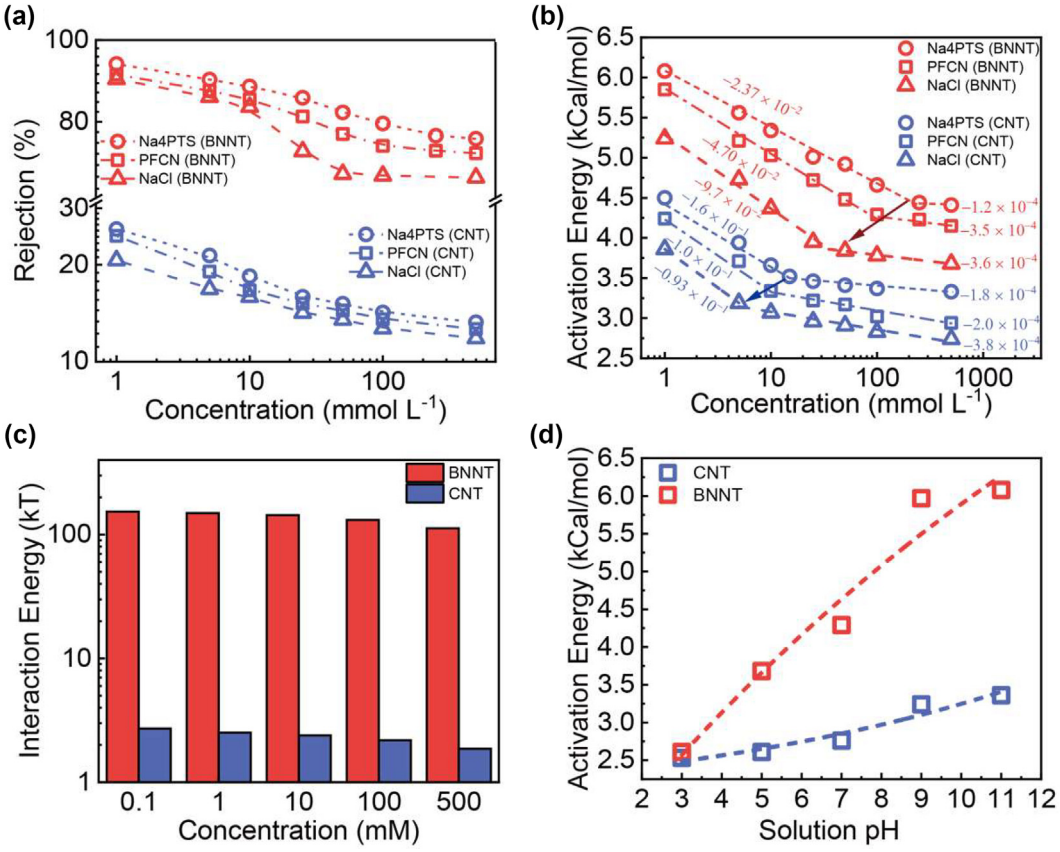

FIGURE 3

(a) Osmotically induced ion rejection for NaCl (open triangles), PFCN (open squares), and Na_4PTS (open circles) as a function of electrolyte concentration (C_{feed} = 0.1 mM to 500 mM) at pH 11. Dotted lines are the best exponential fit. (b) Activation energy (E_a) for the transport of NaCl (open triangles), PFCN (open squares), and Na_4PTS (open circles) through BNNTs and CNTs as a function of the solution concentration (pH 11). (c) Model predictions of DLVO interaction energies between Cl^- anions and the nanotube surface, by adding Van der Waals attraction and electrostatic repulsion for BNNTs (red bar) and CNTs (blue bar). (d) Activation energy (E_a) for the transport of NaCl through BNNTs and CNTs as a function of solution pH (C_{feed} = 10 mM).

Please cite this article in press as: A. Pendse et al., Materials Today (2022), https://doi.org/10.1016/j.mattod.2022.09.006

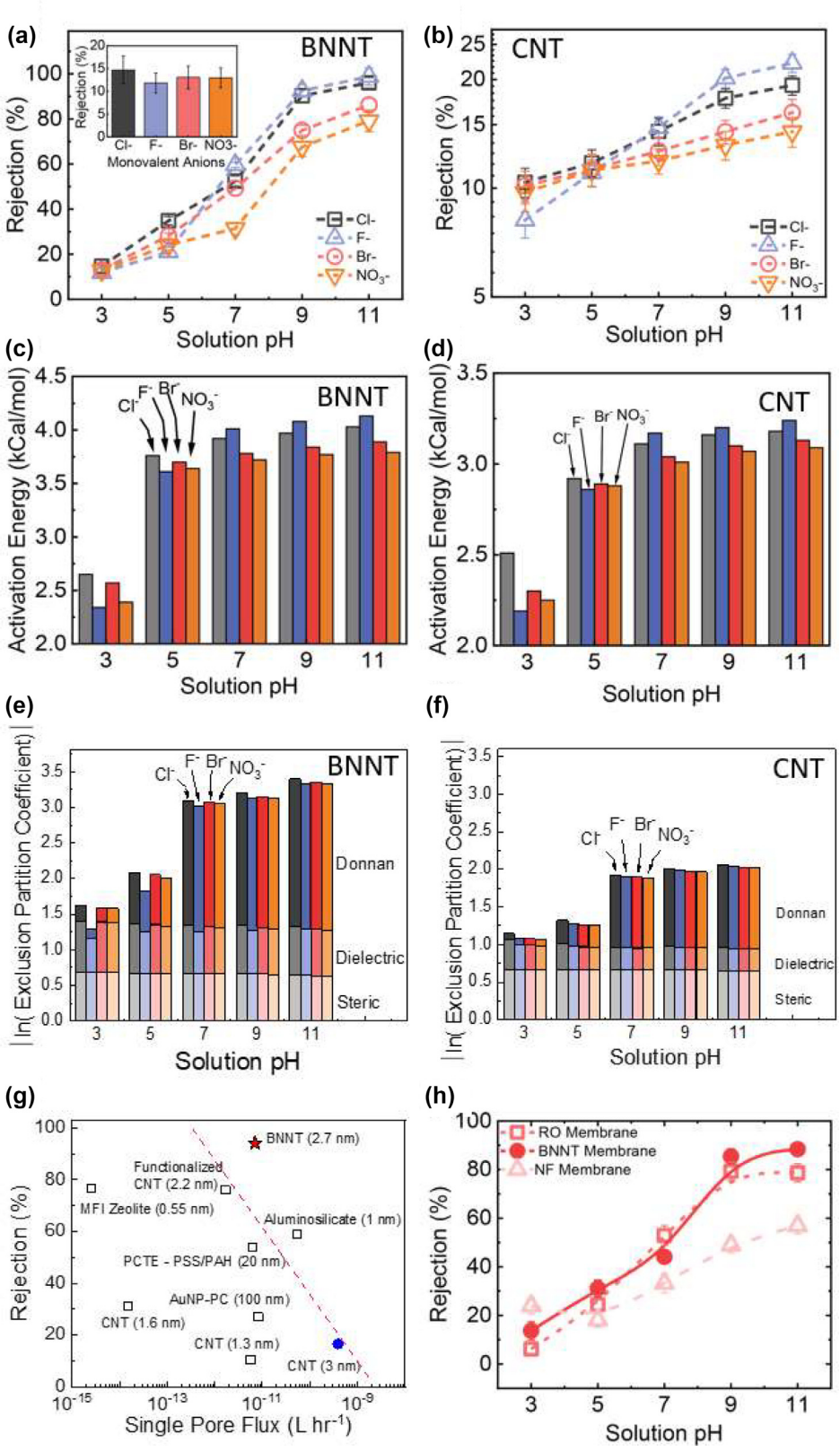

Please cite this article in press as: A. Pendse et al., Materials Today (2022), https://doi.org/10.1016/j.mattod.2022.09.006

ent concentrations. As shown in Fig. 3a, BNNTs showed high ion rejection for the entire tested concentration range: 76–94% (Na_4-PTS), 73–94% (PFCN), and 69–91% (NaCl), whereas the maximum ion rejection by CNTs was only 12–21% (Na_4PTS), 13–25% (PFCN), and 13–26% (NaCl). Fig. 3b shows the changes in the activation energy as a function of the ion concentration and anion valance. Higher activation energy was observed for BNNTs compared with CNTs. Moreover, the transition of the activation energies occurred at 50 mM (NaCl), 100 mM (PFCN), and 250 mM (Na_4PTS) for BNNTs, wherein the slope values for each ion sharply increased from $\approx 10^{-4}$ to $\approx 10^{-2}$. In contrast, CNTs showed the transition at lower concentration ranges of 5 mM (NaCl), 10 mM (PFCN), and 15 mM (Na_4PTS), thus suggesting that the interaction energy between ions and the nanotube surfaces significantly decreased even with a small increase in ion concentration. Additionally, the influence of the surface charge on ion transport (i.e., interaction energy) in BNNTs was evident even at higher concentrations, thus indicating that the screening of BNNT surface charge by cations was not sufficient for easy anion transport through BNNTs. To further quantify the effect of interaction energy on the ion transport mechanism in BNNTs compared with CNTs, we calculated the interaction energy between ions and the nanotube surface by using a surface element integration model and Derjaguin–Landau–Verwey–Overbeek (DLVO) theory, which can estimate Van der Waals and electrostatic double-layer interaction energies [32]. Indeed, the charged BNNT surface showed a high interaction energy barrier for NaCl in the range of 110–150 k_BT, which was higher than that of CNTs (1.86–2.72 k_BT) by two orders of magnitude (Fig. 3c). Furthermore, as depicted in Fig. 3d, the changes in activation energy for the transport of NaCl with the solution pH (pH 3.0–11.0) showed a good correlation with the surface-charge-density values of BNNTs and CNTs (Fig. 1h). The minimum activation-energy value for both CNTs and BNNTs was 2.5 kcal/mol at pH 3, wherein the point of zero charges of the nanotubes and the contribution of the charge-exclusion mechanism was negligible. However, the activation energy for BNNTs increased up to 6.08 kcal/mol at pH 11, whereas the value for CNTs slightly increased, to 3.36 kcal/mol.

To further establish the relationships among the charge densities of ions, surface charge of nanotubes, and ion-transport properties, we systematically investigated the rejection behavior of four monovalent anions, fluoride (F^-), chloride (Cl^-), bromide (Br^-), and nitride (NO_3^-), at different pH values ranging from 3 to 11 (Fig. 4a and 4b). These monatomic ions possess a net charge of −1 and similar hydrated radii but differ in their ionic radii and hydration energy (Table S4). According to dehydration phenomenon theory, ions can temporarily strip and rearrange hydration shells to fit more easily into nanopores (e.g., in nanofiltration membranes), which can differ in ion rejection [24]. The extent of dehydration is closely associated with the hydration energy of these monatomic ions, which in turn greatly depends on ionic sizes (size exclusion) and electrostatic interactions between their charges and the membrane surface (electrostatic repulsion). The results in Fig. 4a and 4b indicated that the four anions showed different rejection by the nanotubes despite having the same ion valence and similar hydrated radii. Both BNNTs (isoelectric point: pH 2.7 [33]) and CNTs (isoelectric point: pH 2 [34]) carried a low surface charge at pH 3 (1.97 mC/m^2 for BNNTs and 0.043 mC/m^2 for CNTs). Thus, the steric-exclusion effects were expected to more strongly govern the transport of monovalent anions in the nanotubes at lower pH conditions. At pH 3, in both BNNTs and CNTs, Cl^-, Br^-, and NO_3^- showed similar rejection values, whereas F^- showed a slightly lower rejection value than the other anions, despite its larger hydrated radius (0.352 nm). This anomaly can be explained by fluorine (F) speciation and the formation of uncharged hydrogen fluoride (HF) at pH < 5, because the pKa of HF is 3.2 [35]. We predicted that the uncharged HF would experience a lower electrostatic repulsion from the neutral (or weakly charged) nanotube surface. Therefore, HF would show lower rejection than the charged Cl^-, Br^- and NO_3^- anions. However, our observations confirmed that even at lower pH conditions, non-negligible contributions from Donnan exclusion effects existed for the BNNT and CNT nanopores. Furthermore, as the solution pH increased, a corresponding increase in the surface-charge density increased the influence of Donnan-exclusion effects, thus resulting in higher anion rejection, as shown in Fig. 4a and 4b. The anion rejection for BNNT pores at pH > 3 followed the order of the hydration energies of the anions, which directly corresponded to their ionic-charge density ($F^- > Cl^- > Br^- > NO_3^-$) (Table S4). At higher pH, the fully speciated F^- ions showed a higher rejection than did Cl^-, Br^- and NO_3^- ions, owing to strong electrostatic repulsion between the BNNT surface and its higher ionic-charge density associated with the markedly small ionic radius. In contrast, CNTs showed a lower rejection of F^- ions at pH < 9.

To further elucidate the monovalent ion transport properties in CNT and BNNT nanopores, we evaluated the change in activation energy for the transport of NaCl, NaF, NaBr, and $NaNO_3$ in response to an increase in the solution pH from 3 to 11 (Fig. 4c and 4d). The activation energy was used to evaluate the influences of multiple mechanisms (e.g., steric hindrance, charge repulsion, and dehydration) limiting ion transport in nanopores. At pH ≤ 5, except for F^-, the activation energies of ion transport in the BNNTs were in the order $Cl^- > Br^- > NO_3^-$, corresponding

FIGURE 4

Various monovalent ion rejection of (a) BNNT and (b) CNT devices at pH 3–11 (C_{feed} = 10 mM): sodium chloride (NaCl), sodium fluoride (NaF), sodium bromide (NaBr), and sodium nitrate ($NaNO_3$). Inset shows rejection for the monovalent ions at pH 3. Activation energy for the transport of Cl–, F–, Br–, and NO_3– through (c) BNNTs and (d) CNTs (C_{feed} = 10 mM). The activation energy is calculated with the Arrhenius equation. Effects of the steric, dielectric, and Donnan effects, calculated with the DSPM–DE model on monovalent ion transport through the (e) BNNTs and (f) CNTs at C_{feed} = 10 mM. (g) NaCl rejection performance of a single BNNT pore compared with other 1D nanopores, in terms of ion rejection and single-pore water-permeation rate. (h) NaCl rejection properties of BNNTs as a function of pH, as compared with those of commercial NF and RO membranes (C_{feed} = 10 mM). Dotted lines represent the best fit to the experimental data.

Please cite this article in press as: A. Pendse et al., Materials Today (2022), https://doi.org/10.1016/j.mattod.2022.09.006

to the order of the hydration energies of the anions (Cl^- > Br^- > NO_3^-), as also seen in Fig. 4a. At a higher pH, ≥ 7, the activation energy of F^- exceeded that of other ions because of the increase in the Donnan-exclusion effect, which correlated with the increase in the surface-charge density. However, in addition to the activation energies of the anions in CNTs being smaller than those in BNNTs, the CNTs showed no distinct differences in activation energies of the anions under most pH conditions, and the changes in the activation energies between pH 3 and 5 were relatively smaller than those in BNNTs (e.g., for NaCl, 43% increase in BNNTs *vs* 16% increase in CNTs), as shown in Fig. 4d. To provide more insight into the ion-rejection properties of BNNTs, we also evaluated the individual contributions of the steric, dielectric, and Donnan-exclusion effects on transport through the nanotubes, by using the DSPM-DE model (Fig. 4e and 4f). The results of the DSPM-DE model indicated that steric and dielectric exclusion dominate the anion transport at lower pH conditions (pH 3 and 5). However, as the pH increases, the resistance to the ion flow increases, owing to the enhanced contributions by Donnan exclusion effects, and thus the activation energies show higher values at high pH. Of note, because the DSPM-DE model considers ion valance rather than ionic-charge density, the Donnan exclusion coefficients for each anion at the same pH were calculated as equal contributions. The contribution of Donnan exclusion in CNT channels also increased with pH, as observed in BNNT channels, although its contribution was smaller than that in BNNTs (2.09 of BNNT *vs* 1.12 of CNT at pH 11), owing to the lower surface-charge density of CNTs.

In Fig. 4g and Table S5, the NaCl separation performance of the 2.7-nm BNNT pores is compared with those of with other 1D nanopore systems, including CNTs, track-etched polycarbonate, aluminosilicate nanotube, and zeolites. Here, we calculated a single-pore flux of the 2.7-nm nanotubes and other nanotube membranes by normalizing the total flux of the nanofluidic platform or membranes with pore density (i.e., number of pores). The 2.7-nm BNNT pores combined very high ion rejection and water permeance, and thus outperformed all other 1D nanopores. Importantly, the NaCl separation performance of other nanopores was within the trade-off curve for NaCl rejection and water flux, whereas the separation performance of BNNTs was far beyond the trade-off curve. We also compared the ion-separation performance of the BNNT device with a commercial RO membrane (Toray Inc., UTC-82V) and NF membrane (Dow Inc., Filmtec–NF270). As shown in Fig. 4h, the 2.7-nm BNNT nanopores demonstrated higher NaCl rejection than the RO (≈0.7 nm) and NF (≈1–2 nm) membranes. The NaCl rejection of BNNT was 1.6 times higher than that of NF (80% of BNNT *vs* 49% of NF at pH 11). Unexpectedly, BNNTs with a pore size approximately 5 times higher than that of the RO membrane exhibited better NaCl rejection performance under higher pH conditions. We observed a similar rejection trend for other monovalent ions (NaF, NaBr, and $NaNO_3$) in Fig. S10, which closely followed the surface-charge-density curve (BNNT > RO > NF) in Fig. S11, thus confirming the major roles of electrostatic effects (Donnan exclusion) on the transport of monovalent ions. The NF membrane (8.89 LMH/bar) showed the highest permeance and was followed by the RO membrane (4.12 LMH/bar) and the BNNT nanofluidic device (0.53 LMH/bar). However, notably, the pore density of the fabricated BNNT device was only ≈10^6 pores/cm^2, a value several orders of magnitude lower than the typical pore density of CNT membranes reported elsewhere [12,36]. By extrapolating the 7.03×10^{-12} L/hr of a single BNNT, we determined that the water permeance of a BNNT membrane with a nanotube density of 10^8–10^{11} pores/cm^2 could range from 20 to 20,000 LMH/bar, indicating several orders of magnitude of enhancement over the NF membranes.

Conclusion

We provide an account of the experimental ion-transport phenomena in ≈2.7-nm BNNTs by using a membrane-like nanofluidic platform. Our BNNT platform showed a significant enhancement of ion rejection over ≈2.7-nm CNT pores with increasing pH and anion valence (z−/z+ ratio), thus strongly suggesting that the stronger electrostatic interactions between highly charged nanotube walls and ionic species play important roles in defining the transport mechanism in BNNT pores. By comparing the experimental results with those of the numerical DSPM-DE and DLVO models, we confirmed that the superior ion-separation properties of BNNT pores stem mainly from Donnan effects (i.e., electrostatic interaction), with minor contributions from steric and dielectric effects. In addition, we demonstrated that monovalent anions with similar hydrated radii are affected to different extents by the charged nanotube surface. BNNTs showed higher rejection properties for anions with higher hydration energies (F^- > Cl^- > Br^- > NO_3^-) at high pH, owing to strong electrostatic interactions resulting from the high surface-charge density of the BNNT wall and ionic-charge density. BNNTs also showed better performance in small-ion separation than commercial RO and NF membranes, despite having a larger pore size. Although further investigation is needed for the successful fabrication of a macroscopic BNNT membrane with high BNNT density, our experimental study provides insights into the effects of surface charge, hydration energy, solution pH, concentration, and ion valence on ion transport in highly charged nanopores, and establishes design criteria for developing highly efficient ion-selective membranes for various practical applications.

CRediT authorship contribution statement

Aaditya Pendse: Investigation, Formal analysis, Writing – original draft. **Semih Cetindag:** Investigation. **Kun Wang:** Investigation, Writing – original draft. **Donglin Li:** Investigation. **Richard J. Castellano:** Investigation. **Da-Chi Yang:** Investigation. **Tongshuai Wang:** Investigation. **Jerry W. Shan:** Conceptualization, Supervision, Writing – review & editing. **Sangil Kim:** Conceptualization, Formal analysis, Supervision, Writing – review & editing.

Data availability

Data will be made available on request.

Declaration of Competing Interest

The authors declare that they have no known competing financial interests or personal relationships that could have appeared to influence the work reported in this paper.

Please cite this article in press as: A. Pendse et al., Materials Today (2022), https://doi.org/10.1016/j.mattod.2022.09.006

Acknowledgements

This work was supported by a grant from the National Science Foundation (Grant No. CMMI-1762905).

Author contributions

A.P. contributed to the nanofluidic device characterization, performance evaluation, theoretical and numerical modelling, and manuscript writing. S.C. contributed to the membrane fabrication and characterization. K.W. contributed to the nanotube characterization and manuscript editing. D.L. contributed to the nanofluidic device performance evaluation. R.C. and D. Yang contributed to the nanotube characterization. T.W. contributed to the nanotube characterization and manuscript editing. J.S. contributed to the concept design and manuscript editing. S.K. contributed to the conceptualization, data analysis, theoretical and numerical modelling, and manuscript writing and editing.

Data availability

The raw/processed data required to reproduce these findings cannot be shared at this time as the data also forms part of an ongoing study.

Appendix A. Supplementary data

Supplementary data to this article can be found online at https://doi.org/10.1016/j.mattod.2022.09.006.

References

[1] L. Bocquet, E. Charlaix, Chem. Soc. Rev. 39 (3) (2010) 1073.
[2] C. Duan, A. Majumdar, Nat. Nanotechnol. 5 (12) (2010) 848.
[3] C.Y. Lee et al., Science 329 (5997) (2010) 1320.
[4] W. Choi et al., Nat. Commun. 4 (2013) 2397.
[5] W. Choi et al., J. Am. Chem. Soc. 133 (2) (2011) 203.
[6] Q. Xie et al., Nat. Nanotechnol. 13 (3) (2018) 238.
[7] W. Jung et al., Adv. Mater. 29 (17) (2017) 1605854.
[8] P. Pang et al., ACS Nano 5 (9) (2011) 7277.
[9] H. Liu et al., Science 327 (5961) (2010) 64.
[10] X. Qin et al., Nano Lett. 11 (5) (2011) 2173.
[11] S. Kim et al., J. Membr. Sci. 460 (2014) 91.
[12] J.K. Holt et al., Science 312 (5776) (2006) 1034.
[13] R.H. Tunuguntla et al., Nat. Nano 11 (7) (2016) 639.
[14] R. Arenal et al., Adv. Phys. 59 (2) (2010) 101.
[15] C.Y. Won, N. Aluru, J. Am. Chem. Soc. 129 (10) (2007) 2748.
[16] E. Secchi et al., Nature 537 (7619) (2016) 210.
[17] M. Wang et al., Nano Lett. 20 (10) (2020) 6937.
[18] A. Pendse et al., Small 15 (49) (2019) 1904590.
[19] C. Chen et al., Nat. Commun. 9 (1) (2018) 1902.
[20] R.J. Castellano et al., J. Appl. Phys. 117 (21) (2015) 214306.
[21] R.J. Castellano et al., Carbon 157 (2020) 208.
[22] R.M. Smeets et al., Nano Lett. 6 (1) (2006) 89.
[23] A. Siria et al., Nature 494 (7438) (2013) 455.
[24] R. Epsztein et al., Environ. Sci. Technol. 52 (7) (2018) 4108.
[25] L. Jiang, L. Gao, J. Mater. Chem. 15 (2) (2005) 260.
[26] S. Bhattacharjee, M. Elimelech, J. Colloid Interface Sci. 193 (2) (1997) 273.
[27] B. Tansel et al., Sep. Purif. Technol. 51 (1) (2006) 40.
[28] D. Stein et al., Phys. Rev. Lett. 93 (3) (2004) 035901.
[29] S. Li et al., Environ. Sci.: Processes Impacts 21 (12) (2019) 2109.
[30] P. Krishnakumar et al., Nanotechnology 23 (45) (2012) 455101.
[31] F.G. Donnan, Chem. Rev. 1 (1) (1924) 73.
[32] M. Zhang et al., Nat. Commun. 10 (1) (2019) 1253.
[33] C. Xiong, W. Tu, Eur. J. Inorg. Chem. 2014 (19) (2014) 3010.
[34] D. Heltina et al., J. Phys. 1351 (2019) 012090.
[35] L.A. Richards et al., Desalination 261 (3) (2010) 331.
[36] B. Lee et al., Nat. Commun. 6 (1) (2015) 1.

Please cite this article in press as: A. Pendse et al., Materials Today (2022), https://doi.org/10.1016/j.mattod.2022.09.006